Acta Crystallographica Section D
Biological Crystallography
ISSN 0907-4449

Structural insight into plant programmed cell death mediated by BAG proteins in *Arabidopsis thaliana*

Shasha Fang,[a,b] Luhua Li,[b] Boyang Cui,[a,b] Shuzhen Men,[b]* Yuequan Shen[a,b]* and Xue Yang[a]*

[a]State Key Laboratory of Medicinal Chemical Biology, Nankai University, Tianjin 300071, People's Republic of China, and [b]College of Life Sciences, Nankai University, Tianjin 300071, People's Republic of China

Correspondence e-mail: shuzhenmen@nankai.edu.cn, yshen@nankai.edu.cn, yangxue@nankai.edu.cn

Received 14 November 2012
Accepted 5 February 2013

PDB References: AtBAG1 BD, 4hwc; AtBAG2 BD, 4hwd; AtBAG3 BD, 4hwf; AtBAG4 BD, 4hwh; AtBAG1 UBD–NBD complex, 4hwi

The recently identified plant Bcl-2-associated athanogene (BAG) family plays an extensive role in plant programmed cell death (PCD) processes ranging from growth and development to stress responses and even cell death. In the *Arabidopsis thaliana* BAG (AtBAG) protein family, four members (AtBAG1–4) have a domain organization similar to that of mammalian BAG proteins. Here, crystal structures of the BAG domains (BDs) of AtBAG1–4 have been determined; they have high homology and adopt a structure comprising three short parallel α-helices, similar to some mammalian BAG proteins. The crystal structure of a complex of the AtBAG1 ubiquitin-like domain and BAG domain (UBD) with the Hsc70 nucleotide-binding domain (NBD) was also determined. The binding of the AtBAG1 BD to the Hsc70 NBD induces conformational change of the Hsc70 NBD to the open state and reduces the affinity of the NBD for ADP. *In vivo* studies showed that *bag2-1* mutant plants are larger than wild-type plants when growing under normal conditions, indicating that the AtBAG proteins might regulate plant PCD and confer tolerance to stresses in plants. These structural and functional analyses indicate that the AtBAG proteins function as nucleotide-exchange factors for Hsp70/Hsc70 in *A. thaliana* and that the mechanism of regulation of chaperone-mediated protein folding is conserved in plants.

1. Introduction

Programmed cell death (PCD) plays a critical role throughout the entire life of plants (Pennell & Lamb, 1997). PCD is indispensable for tissue expression, organ construction and function. PCD is also likely to occur during the vegetative and reproductive phases of plant development (Kuriyama & Fukuda, 2002). Plants are challenged by various abiotic and biotic stresses owing to their nonmotile nature. Studies have proven that regulation of PCD is an essential plant defence strategy (Panter & Dickman, 2005). Recently, a protein family, the Bcl-2-associated athanogene (BAG) family, was identified as comprising regulators of plant PCD. Seven members of the *Arabidopsis thaliana* BAG family have been identified (AtBAG1–7). They all contain a common C-terminal BAG domain (BD). The AtBAG proteins are diversely located in the cytosol, endoplasmic reticulum, mitochondria and nucleus (Doukhanina *et al.*, 2006). *In vivo* studies have revealed that the AtBAG proteins are multifunctional as they regulate diverse processes, including growth, development and even cell death. The AtBAG family members have been found to

inhibit plant PCD pathways in response to stress. It has been reported that AtBAG4 is involved in a wide range of abiotic defences, including those against salt, cold, drought and oxidants (Doukhanina *et al.*, 2006), while AtBAG6 has an effect on host defence against pathogen attack and the regulation of cell-death processes (Kang *et al.*, 2006). Recent data have demonstrated that AtBAG7 localizes to the endoplasmic reticulum (ER) and plays a role in ER stress responses as a cochaperone (Williams *et al.*, 2010). The mechanism of the pathway mediated by AtBAG proteins and the identification of their binding partners are of considerable interest.

The BAG proteins were first discovered in mammals in a search for Bcl-2-interacting proteins. The BAG proteins have been shown to promote cell survival (Takayama *et al.*, 1995). Extensive studies have demonstrated that some mammalian BAG proteins function as nucleotide-exchange factors for heat-shock protein 70 (Hsp70) *via* the BD. The stress-induced chaperone Hsp70 and its highly homologous constitutively expressed counterpart Hsc70 play a critical role in protein folding and cellular stress responses (Mayer & Bukau, 2005). Hsp70 and Hsc70 are composed of an N-terminal nucleotide-binding domain (NBD) and a C-terminal substrate-binding domain (SBD). The three-dimensional structures of mammalian BDs vary and include the three nearly parallel long helices adopted by BAG1 (Sondermann *et al.*, 2001), the dimeric three nonparallel α-helices of BAG2 (Xu *et al.*, 2008) and the shorter three-α-helix bundle adopted by BAG3, BAG4, the first BAG domain of BAG5 (BAG5 BD1), BAG5 BD4 and BAG5 BD5 (Arakawa *et al.*, 2010). The Hsp70/Hsc70 binding modes of mammalian BDs are also distinct. BAG5 BD1 and BAG5 BD4 are not known to have NBD-binding ability, although their structures are almost the same as that of BAG5 BD5 (Arakawa *et al.*, 2010). BAG1 BD and BAG5 BD5 bind to the NBD in a similar manner; both induce the open NBD state and facilitate ADP release (Sondermann *et al.*, 2001; Arakawa *et al.*, 2010). BAG2 BD also facilitates nucleotide exchange but adopts a distinct NBD-binding mode (Xu *et al.*, 2008). The diversity of BDs raises interest in the three-dimensional structures and Hsp70/Hsc70-binding mode of plant BAG proteins.

The AtBAG family members can be divided into at least two groups. The first group is composed of AtBAG1–4. AtBAG1, AtBAG2, AtBAG3 and AtBAG4 are composed of 326, 302, 303 and 269 amino-acid residues, respectively. As in mammalian BAG1, they all include a characteristic C-terminal BD and a ubiquitin-like domain (ULD) at the N-terminus. AtBAG5–7, which are composed of 215, 1043 and 446 amino-acid residues, respectively, contain a conserved IQ motif located immediately before the BD. In the present study, we determined the crystal structures of the AtBAG1–4 BDs, which all adopt the shorter monomeric three parallel α-helix bundle structure and act as nucleotide-exchange factors for Hsp70/Hsc70. We also determined the crystal structure of a complex of the AtBAG1 ubiquitin-like domain and BAG domain (UBD) with the Hsc70 NBD and characterized its similarity to the mammalian BAG1 BD–NBD complex and the mammalian BAG5 BD5–NBD complex.

2. Materials and methods

2.1. Protein expression and purification

Gene fragments encoding the AtBAG1 BD (residues 157–242), AtBAG1 UBD (residues 66–242), AtBAG2 BD (residues 129–214), AtBAG3 BD (residues 135–220), AtBAG4 BD (residues 138–223) and human Hsc70 NBD (residues 5–387) were PCR-amplified and confirmed by DNA sequencing. The recombinant proteins were expressed in *Escherichia coli* BL21 CodonPlus cells at 298 K for 16–18 h. The AtBAG1 BD, AtABAG2 BD, AtBAG3 BD, AtBAG4 BD and NBD were prepared as N-terminal His_6-fusion proteins and purified by Ni^{2+}–NTA agarose (Qiagen) affinity chromatography. After digestion with PreScission Protease to cleave the N-terminal His_6 tag, contaminants were removed by a second Ni^{2+}–NTA agarose affinity-chromatography step followed by HiLoad 26/60 Superdex 200 (GE Healthcare) size-exclusion chromatography. MBP-tagged AtBAG1 UBD expressed in bacterial cells was purified using an MBPTrap HP column (GE Healthcare) followed by TEV protease digestion. The cleaved tag was removed by ion-exchange chromatography on a Mono S column. The AtBAG1 UBD–NBD complex was formed by mixing the separately purified proteins together and passing the solution through the size-exclusion chromatography column.

Methylation of AtBAG3 BD was performed as described in Rayment (1997). The methylation reaction was performed overnight in 20 m*M* Tris pH 7.5, 200 m*M* NaCl, 5% glycerol at a protein concentration of 1 mg ml^{-1}. 20 µl freshly prepared 1 *M* dimethylamine–borane complex (ABC; Fluka product No. 15584) and 40 µl 1 *M* formaldehyde (made from 37% stock; Fluka product No. 33220) were added per millilitre of protein solution and the reactions were gently mixed and incubated at 277 K for 2 h. A further 20 µl ABC and 40 µl formaldehyde were added and incubation was continued for a further 2 h. Following a final addition of 10 µl ABC, the reaction was incubated overnight at 277 K. After methylation, 5 mg glycine and 5 m*M* DTT were added to the solution. The methylated AtBAG3 BD was purified using a size-exclusion chromatography column.

SeMet-derivatized AtBAG3 BD and AtBAG4 BD proteins were produced following the same protocol as was used for the wild-type protein, with the exception that methionine-auxotroph *E. coli* B834 (DE3) cells and minimal medium were used to express the recombinant proteins.

2.2. Crystallization and data collection

All crystals were grown using sitting-drop vapour diffusion. The AtBAG1 BD protein was crystallized by combining 1 µl protein solution (20 mg ml^{-1} in 20 m*M* Tris–HCl pH 7.5, 200 m*M* NaCl, 1 m*M* DTT, 1 m*M* EDTA) with an equal volume of well solution consisting of 0.2 *M* NaCl, 0.1 *M* Tris–HCl pH 8.5, 32% PEG 3350. The crystals were grown for approximately one week at 277 K and were cooled in cryoprotectant consisting of well solution supplemented with 25% glycerol. The AtBAG2 BD was crystallized by combining 1 µl protein solution (10 mg ml^{-1} in 20 m*M* Tris–HCl pH 7.5,

Table 1
Data-collection and refinement statistics for the AtBAG protein structures.

Values in parentheses are for the highest resolution shell.

Crystal name	AtBAG1	AtBAG2	AtBAG3	AtBAG4	AtBAG1 UBD–NBD
Space group	$P2_12_12_1$	$P2_12_12_1$	$P3_221$	$P2_12_12_1$	$P2_1$
Unit-cell parameters (Å, °)	a = 56.72, b = 96.85, c = 103.01	a = 26.14, b = 60.45, c = 177.03	a = b = 55.69, c = 173.55	a = 63.66, b = 73.33, c = 111.63	a = 61.93, b = 87.36, c = 65.07, β = 109.18
Wavelength (Å)	0.9795	0.9792	0.9795	0.9795	0.9795
Resolution range (Å)	50.00–1.80 (1.84–1.80)	50.00–2.30 (2.35–2.30)	50.00–1.78 (1.81–1.78)	50.00–1.90 (1.94–1.90)	50.00–2.27 (2.35–2.27)
Unique reflections	53148	13030	30454	40136	29513
Completeness (%)	98.5 (96.9)	98.4 (95.3)	95.3 (78.8)	98.6 (72.1)	92.0 (90.9)
Multiplicity†	7.1 (4.7)	5.8 (6.2)	8.5 (3.0)	6.9 (4.5)	3.3 (3.0)
R_{merge}‡ (%)	5.4 (47.9)	4.1 (11.7)	4.9 (36.3)	2.3 (37.1)	3.9 (9.5)
$\langle I/\sigma(I)\rangle$	25.6 (1.9)	27.4 (14.6)	32.6 (2.2)	63.1 (3.0)	26.5 (12.8)
Refinement					
$R_{crystal}$§ (%)	23.8	23.1	21.8	20.7	20.3
R_{free}¶ (%)	25.1	25.3	24.5	23.6	25.9
R.m.s.d. from ideal					
Bond lengths (Å)	0.006	0.006	0.008	0.005	0.007
Bond angles (°)	0.959	0.984	0.841	0.609	1.008
No. of atoms					
Protein	3864	2023	1270	3290	4307
Ligand	4	0	10	36	0
Solvent	543	182	141	261	114

† N_{obs}/N_{unique}. ‡ $R_{merge} = \sum_{hkl}\sum_i |I_i(hkl) - \langle I(hkl)\rangle|/\sum_{hkl}\sum_i I_i(hkl)$, where $I_i(hkl)$ is the intensity of the ith reflection and $\langle I(hkl)\rangle$ is the average intensity. § $R_{crystal} = \sum_{hkl}||F_{obs}| - |F_{calc}||/\sum_{hkl}|F_{obs}|$. ¶ R_{free} is calculated in the same way as $R_{crystal}$ but from a test set containing 5% of the data, which were excluded from the refinement calculation.

Table 2
Data-collection and refinement statistics for the SeMet-derivative AtBAG protein structures.

Values in parentheses are for the highest resolution shell.

Crystal name	SeMet AtBAG3	SeMet AtBAG4
Space group	$P3_221$	$P2_12_12_1$
Unit-cell parameters (Å)	a = b = 55.81, c = 173.52	a = 63.69, b = 72.28, c = 110.72
Wavelength (Å)	0.9795	0.9795
Resolution range (Å)	50.00–2.00 (2.07–2.00)	50.00–3.00 (3.05–3.00)
No. of unique reflections	22051	10767
Multiplicity	9.5 (3.3)	12.9 (6.5)
R_{merge}† (%)	7.4 (36.9)	5.5 (24.0)
$\langle I/\sigma(I)\rangle$	63.7 (2.9)	65.8 (4.5)
Completeness (%)	99.4 (95.3)	93.3 (84.9)

† $R_{merge} = \sum_{hkl}\sum_i |I_i(hkl) - \langle I(hkl)\rangle|/\sum_{hkl}\sum_i I_i(hkl)$, where $I_i(hkl)$ is the intensity of the ith reflection and $\langle I(hkl)\rangle$ is the average intensity.

200 m*M* NaCl, 1 m*M* DTT, 1 m*M* EDTA) with an equal volume of well buffer consisting of 0.2 *M* ammonium sulfate, 20% PEG 3350. The crystals were grown over one week at 293 K and cooled in cryoprotectant consisting of well solution supplemented with 25% glycerol. Methylated AtBAG3 BD was crystallized by combining 1 µl protein solution (10 mg ml^{-1} in 20 m*M* Tris–HCl pH 7.5, 200 m*M* NaCl, 1 m*M* DTT, 1 m*M* EDTA) with an equal volume of well buffer consisting of 0.1 *M* HEPES pH 7.5, 1.7 *M* lithium sulfate. The crystals were grown over one week at 277 K and cooled directly. The AtBAG4 BD was crystallized by combining 1 µl protein solution (20 mg ml^{-1} in 20 m*M* Tris–HCl pH 7.5, 200 m*M* NaCl, 1 m*M* DTT, 1 m*M* EDTA) with an equal volume of well buffer consisting of 10% Tacsimate pH 5.0, 20% PEG 3350. The crystals were grown over one week at 293 K and cooled in cryoprotectant consisting of well solution supplemented with 25% glycerol. The AtBAG1 UBD–NBD complex was crystallized by combining 1 µl protein solution (20 mg ml^{-1} in 20 m*M* Tris–HCl pH 7.5, 200 m*M* NaCl, 1 m*M* DTT, 1 m*M* EDTA) with an equal volume of well buffer consisting of 0.02 *M* citric acid, 0.08 *M* bis-tris propane pH 8.8, 20% PEG 3350. The crystals were grown over one week at 277 K and cooled in cryoprotectant consisting of well solution supplemented with 25% glycerol. SeMet-substituted crystals of AtBAG3 BD and AtBAG4 BD were produced using the same method as used for the wild-type crystals.

All data were collected on the BL17U1 beamline at the Shanghai Synchrotron Radiation Facility (SSRF) and were processed using the *HKL*-2000 suite (Otwinowski & Minor, 1997). Single-wavelength anomalous data were collected from the SeMet-substituted crystals at the Se peak wavelength on the BL17U1 beamline at SSRF.

2.3. Structure determination and refinement

The crystal structure of the AtBAG4 BD was determined using the SAD methodology. The program *HKL2MAP* (Pape & Schneider, 2004) was used to search for the Se sites and the initial phases were then calculated using the *PHENIX* software (Adams *et al.*, 2010). The model was built manually using the program *Coot* (Emsley & Cowtan, 2004). After the initial main-chain model had been built, the wild-type data were used to carry out an iterative refinement to assign all side chains using *PHENIX* until the free *R* factor converged. Noncrystallographic symmetry (NCS) restraints were applied at the beginning of the refinement and were removed at a later stage of the refinement of the AtBAG4 BD structure. The initial phase of the structure of the AtBAG1 BD was obtained by molecular replacement using the program *Phaser* (McCoy

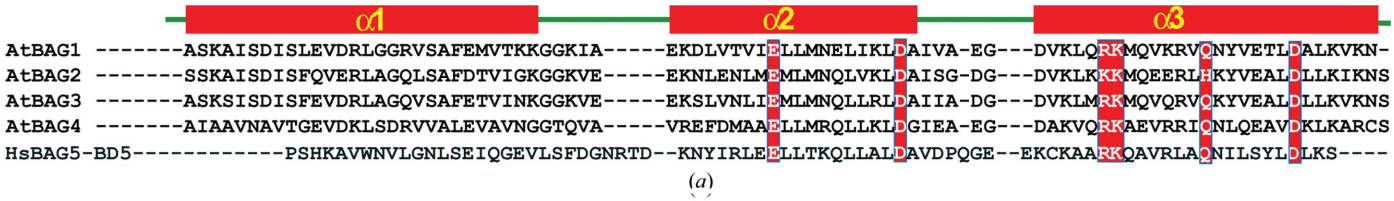

(*a*)

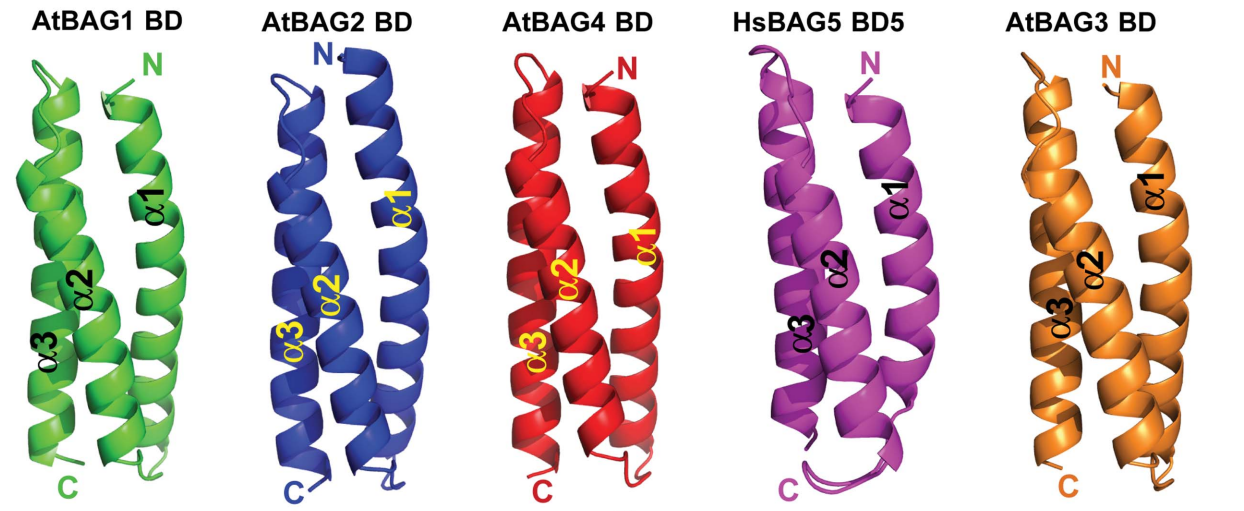

(*b*)

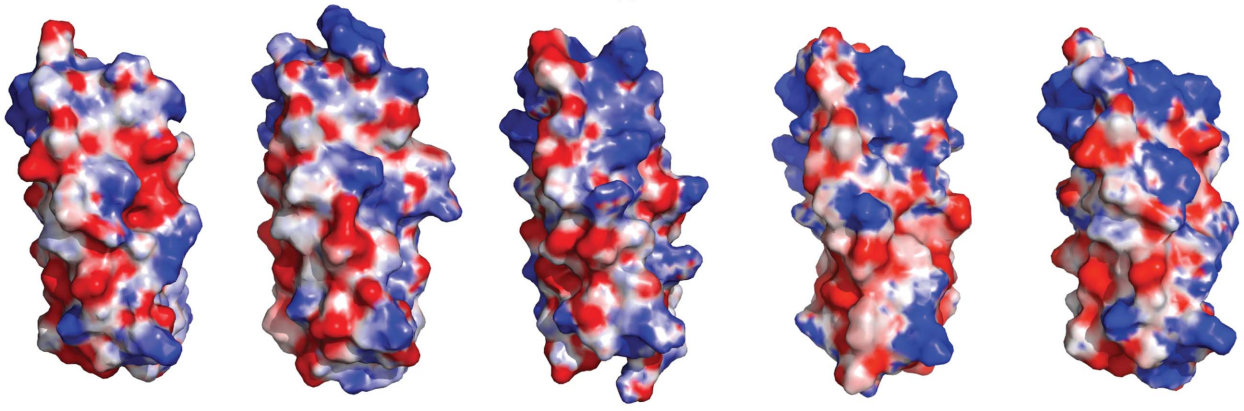

(*c*)

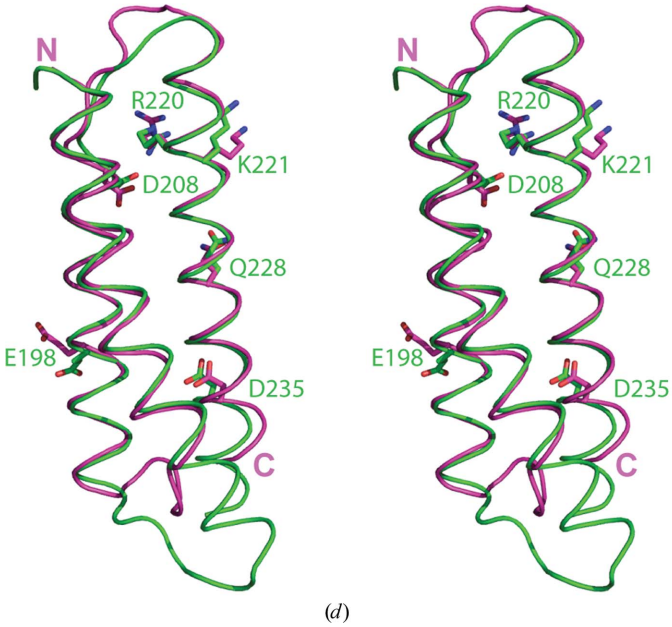

(*d*)

Figure 1
Overall structures of the BAG domains of AtBAG1–4. (*a*) Structure-based sequence alignment of the AtBAG1–4 BDs and mammalian BAG5 BD5 (HsBAG5 BD5). The highly conserved residues critical in Hsp70/Hsc70 binding are boxed in red. The locations of the three helices are shown above the alignment. (*b*) The overall structures of the AtBAG1 BD, AtBAG2 BD, AtBAG4 BD and HsBAG5 BD5 (PDB entry 3a8y) and the model of the AtBAG3 BD are shown in green, blue, red, magenta and orange, respectively. (*c*) Electrostatic potential maps of the AtBAG1 BD, AtBAG2 BD, AtBAG4 BD, HsBAG5 BD5 and AtBAG3 BD. (*d*) Stereoview of the structural alignment of the AtBAG1 BDs and the HsBAG5 BD5. Several key residues in the chaperone interaction are displayed as sticks.

Table 3
Primers used for AtBAG2 studies *in vivo*.

Primer name	Primer sequence (5′–3′)	Use
LBa1	TGGTTCACGTAGTGGGCCATC	T-DNA specific primer
BAG2_F1_667	GGAGGGAAAGTTGAAGAGAAGA	Genotyping of *bag2-1*and RT-PCR
BAG2_R1_1888	TGCTGGATGTTGACGACATGTT	Genotyping of *bag2-1*
APT1-F	GTTGAATGTGCTTGCG	RT-PCR references
APT1-R	CTTTAGCCCCTGTTGG	RT-PCR references
BAG2_R2_1415	CGACCAATCACAAATCATATACA	RT-PCR

et al., 2007). The AtBAG4 BD structure was used as the search model. Six molecules in one asymmetric unit were successfully found by the software. The models were built using *Coot* and refined using *PHENIX*. NCS restraints were used at the beginning of the refinement and were removed at a later stage. A simulated-annealing procedure was performed in the first run of the refinement. Iterative cycles of positional and *B*-factor refinement were carried out until the free *R* factor converged. The AtBAG2 BD structure was solved and refined by following a similar strategy to that used for the AtBAG1 BD except that three molecules were found in the symmetric unit. The structure of the AtBAG3 BD was determined using the SAD methodology as described for the AtBAG4 BD. The structure of the AtBAG1 UBD–NBD complex was initially solved by molecular replacement using the structures of the AtBAG1 BD and the NBD in the BAG1 BD–Hsc70 NBD complex (PDB entry 1hx1; Sondermann *et al.*, 2001) as models using *Phaser*. Structure refinement was performed with *PHENIX*. Detailed data-collection and refinement statistics are summarized in Tables 1 and 2. The surface electrostatics of each structure were calculated using the program *APBS* (Baker *et al.*, 2001).

2.4. Glutathione *S*-transferase (GST) pull-down assay

Gene fragments encoding the BDs of AtBAG1–4 were cloned into pHGB.HA, an in-house-modified vector based on the pET32a vector (Novagen) containing fragments encoding haemagglutinin (HA) and the B1 domain of the streptococcal protein GB1, and expressed in *E. coli* BL21 CodonPlus cells. The NBD of *A. thaliana* Hsc70 (residues 1–387; AtHsc70 NBD) was cloned into the pET-GST vector (Novagen). *E. coli* cells harbouring the GST-fused AtHsc70 NBD were grown at 310 K to an OD_{600} of 0.6. The culture was shifted to 321 K for 2 h and then transferred to 298 K for 16–18 h. The target protein was purified using glutathione-affinity chromatography.

Purified GST-fused AtHsc70 NBD was first immobilized on 15 µl of Glutathione Sepharose 4B beads (GE Healthcare) at 277 K for 2 h. 500 µl of cell lysate containing overexpressed GB1-HA-fused AtBAG BD protein was then added. Binding was allowed to proceed at 277 K with rocking for a further 2 h. The beads and bound materials were then washed extensively with buffer consisting of 20 m*M* Tris–HCl pH 7.5, 400 m*M* NaCl, 1 m*M* EGTA, 1 m*M* DTT, 5% glycerol, 0.5% Triton X-100. The bound proteins were boiled in SDS sample loading dye buffer, separated by SDS–PAGE (15% polyacrylamide) and subsequently analyzed by immunoblotting using anti-HA antibodies. In the gradient pull-down assay, the same amount of GST-fused AtHsc70 NBD was loaded onto beads of the same volume, while the lysate inputs containing the AtBAG1 BD or AtBAG1 UBD were gradually increased from 20 to 40, 100 and 300 µl.

2.5. ITC measurements

The interaction between the NBD and ADP was monitored using ITC measurements (Wiseman *et al.*, 1989) performed at 293 K using an ITC-200 microcalorimeter (MicroCal). The samples were buffered with 20 m*M* Tris–HCl buffer pH 8.0 containing 200 m*M* NaCl and 5 m*M* $MgCl_2$. Aliquots of a 400 µ*M* ADP solution (in the syringe) were stepwise injected into 20 µ*M* NBD solution with or without equal amounts of the AtBAG BD or the AtBAG1 UBD (in the cell). To measure the binding constants of the NBD for the AtBAG1 BD or the AtBAG1 UBD, aliquots of 500 µ*M* AtBAG BD or AtBAG UBD (in the syringe) were stepwise injected into 50 µ*M* NBD solution (in the cell). The data were analyzed with the MicroCal *Origin* software using a binding model that assumed a single site of interaction.

2.6. Analytical ultracentrifugation

Sedimentation velocity was determined in a Beckman/Coulter XL-1 analytical ultracentrifuge using double-sector centrepieces and sapphirine windows. The sample was prepared in 20 m*M* Tris–HCl, 200 m*M* NaCl pH 8.0. The experiment was conducted at 42 000 rev min^{-1} and 293 K using interference detection and double-sector cells loaded with approximately 20 mg ml^{-1} protein. The buffer composition (density and viscosity) and the protein partial specific volume ($\bar{V}$) were determined using the *SEDNTERP* program (available through the Boston Biomedical Research Institute). The data were analyzed using the *SEDFIT* and *SEDPHAT* programs (Schuck, 2000).

2.7. Plant materials and growth conditions

A *bag2-1* T-DNA insertion-mutant line in the Columbia (Col-0) background from the SALK collection was obtained from the *Arabidopsis* Biological Resource Center (ABRC) with stock number SALK_030295. The T-DNA insertion was confirmed by PCR using the primers listed in Table 3. BAG2 transcription levels were determined by semi-quantitative RT-PCR; the primers used are listed in Table 3. Seeds were stratified at 277 K for 3–4 d in the dark. Seedlings were grown

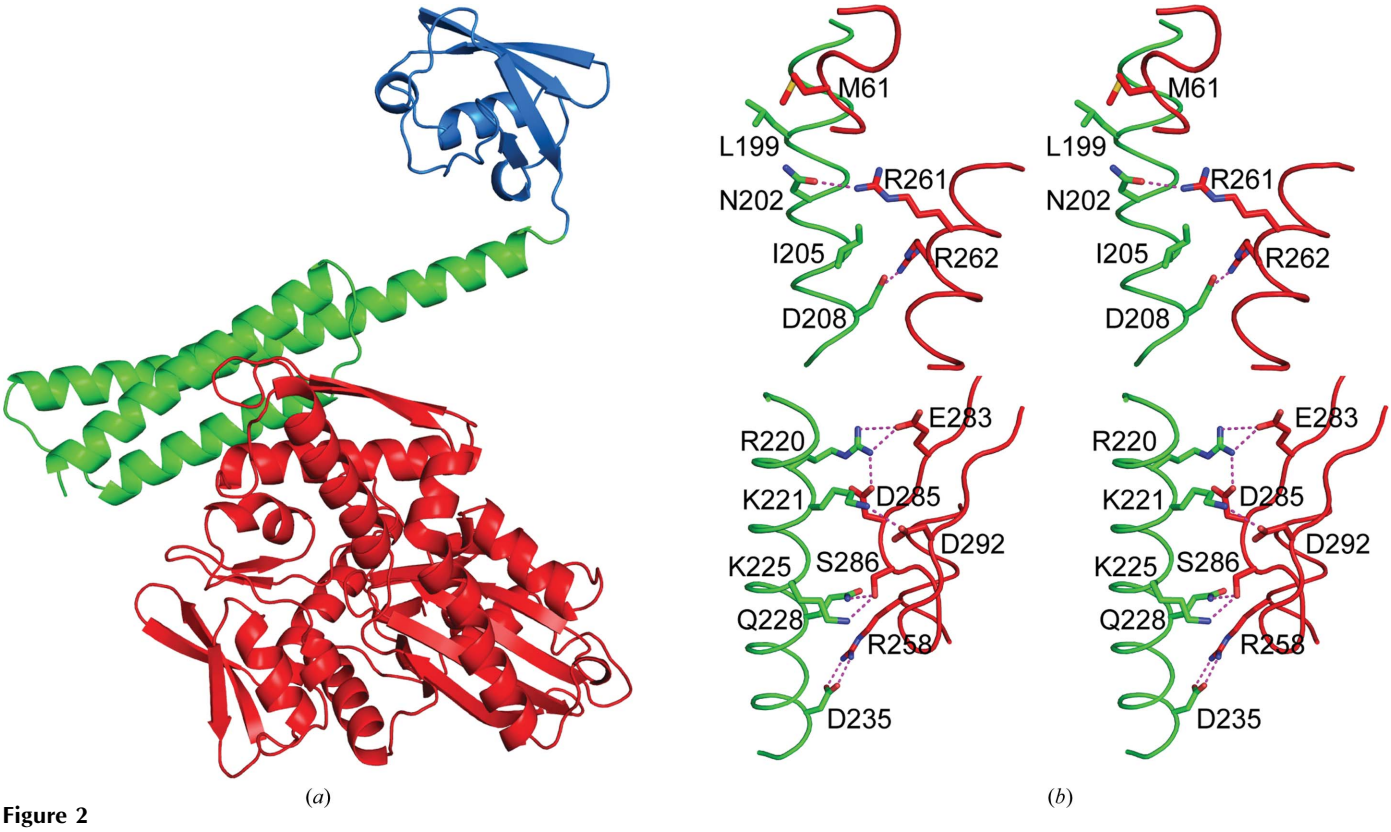

Figure 2
Structure of the AtBAG1 UBD in complex with the NBD. (*a*) The overall structure of the AtBAG1 UBD–Hsc70 NBD complex. The ULD, BD and NBD are coloured marine, green and red, respectively. (*b*) The detailed interactions between the AtBAG1 UBD and the NBD. The AtBAG1 UBD is coloured green and the NBD is coloured red. Hydrogen bonds are shown as magenta dashed lines.

vertically on MS medium. Plants were grown under a 16 h light/8 h dark cycle at 293–296 K.

2.8. Protein Data Bank accession codes

The atomic coordinates and structure factors have been deposited in the Protein Data Bank with accession codes 4hwc for the AtBAG1 BD, 4hwd for the AtBAG2 BD, 4hwf for the AtBAG3 BD, 4hwh for the AtBAG4 BD and 4hwi for the AtBAG1 UBD–NBD complex.

3. Results

3.1. The overall structures of the AtBAG1–4 BDs

The primary sequences of the AtBAG1–4 BDs are highly conserved (Fig. 1*a*). The AtBAG1 BD exhibits 59.8, 73.3 and 44.2% amino-acid identity to the AtBAG2, AtBAG3 and AtBAG4 BDs, respectively. We first successfully crystallized residues 138–223 of AtBAG4 and solved the corresponding BD structure using single-wavelength anomalous dispersion (SAD) at a resolution of 1.9 Å. The AtBAG4 BD crystals belonged to the orthorhombic space group $P2_12_12_1$, with five independent molecules in each asymmetric unit. The crystal structures of the AtBAG1 BD (residues 157–242) and the AtBAG2 BD (residues 129–214) were determined to resolutions of 1.8 and 2.3 Å, respectively, by molecular replacement using the AtBAG4 BD as the model. The AtBAG1 BD and AtBAG2 BD crystals are both orthorhombic, with six and three independent molecules per asymmetric unit, respectively. No significant differences were observed among the molecules in the asymmetric unit. The overall topology of the AtBAG1, AtBAG2 and AtBAG4 BDs is strikingly similar, consisting of three antiparallel α-helices (Fig. 1*b*). The root-mean-square derivations (r.m.s.d.s) of the AtBAG2 BD and AtBAG4 BD structures from the AtBAG1 BD structure are 0.72 and 0.84 Å, respectively. The structures also share a very similar electron-potential distribution on the protein surface (Fig. 1*c*).

The AtBAG3 BD (residues 135–220) structure was solved using SAD to a resolution of 1.8 Å. The space group was identified as $P3_221$. The asymmetric unit contained two molecules with different conformations, which are designated molecule *A* and molecule *B* (Supplementary Fig. S1*a*[1]). Molecule *A* does not intact with the 11 amino acids that are missing between helix α1 and helix α2. Its overall topology is significantly different from those of the other AtBAG BDs. In molecule *B*, helix α1 and helix α2 assume almost the same overall structures as that of the AtBAG1 BD, with an r.m.s.d. value of 0.82 Å (Supplementary Fig. S1*b*); however, the location of helix α3 has been assumed by helix α2 from

[1] Supplementary material has been deposited in the IUCr electronic archive (Reference: DW5039). Services for accessing this material are described at the back of the journal.

molecule *A*. This abnormal conformation is most likely to be an artifact induced by the lysine methylation of the AtBAG3 BD. The reductive methylation of lysine residues has been proven to enhance crystal packing by changing the protein surface properties and introducing more protein–protein interactions (Walter *et al.*, 2006). Based on the high sequence identity of the AtBAG3 BD to the AtBAG1 BD, it is possible that the overall structure of the AtBAG3 BD is similar to those of the other AtBAG BDs. The model generated by *SWISS-MODEL* (Arnold *et al.*, 2006; Kiefer *et al.*, 2009), which shows an antiparallel three-helix bundle, might represent the authentic structure of the AtBAG3 BD (Fig. 1*b*).

The AtBAG BDs, represented by the AtBAG1 BD, were compared with structurally characterized mammalian BDs (Supplementary Fig. S2). Compared with the new BAG (BNB) structure of BAG2, the AtBAG BDs are more structurally similar to the three-helix bundle of the BAG1, BAG3, BAG4 and BAG5 BDs. Among these BDs, BAG5 BD5 presented the highest primary sequence homology to AtBAG1 BD (24.2%). High similarity with respect to electron-potential distribution on the protein surface was found between BAG5 BD5 and the AtBAG BDs (Fig. 1*c*). The BAG5 BD5 structure could be superimposed well on the AtBAG1 BD structure. The position and conformation of the residues critical in BAG5 BD5–Hsc70 NBD binding are conserved in the AtBAG BDs (Fig. 1*d*).

3.2. Crystal structure of the AtBAG1 UBD–NBD complex

Our next goal was to address the effect of BAG proteins on the chaperone Hsp70/Hsc70 in plants. The Hsc70 NBD is highly conserved between human and *A. thaliana*, with a sequence identity of 81.4%. Owing to the failure to crystallize the *A. thaliana* Hsc70 (AtHsc70) NBD in the *E. coli* system, we cocrystallized the AtBAG1 UBD (residues 66–242 containing both the ULD and the BD) with the human Hsc70 NBD (residues 5–387) and solved the complex structure at a resolution of 2.3 Å. The asymmetric unit of the crystal contained one molecule of the complex, in which only the BD was responsible for the interaction with the NBD (Fig. 2*a*). The details of the contact interface are shown in Fig. 2(*b*). Helices α2 and α3 of the BD of AtBAG1 make an extensive contact with the Hsc70 NBD. The side chain of Leu199 in helix α2 of the AtBAG1 BD makes a hydrophobic contact with Met61 of the NBD. A hydrogen bond is formed between the side chain of Asn202 in helix α2 and Arg261 of the NBD. The side chain of Arg262 of the NBD forms a salt bridge with the side chain of Asp208 and also hydrophobically contacts Ile205 in helix α2. In helix α3, residues including Arg220, Lys221, Lys225, Gln228 and Asp235 form comprehensive interactions with residues in the NBD. These extensive contacts are very similar to those in the BAG1–Hsc70 NBD (Sondermann *et al.*, 2001) and BAG5 BD5–Hsp70 NBD (Arakawa *et al.*, 2010) complex structures.

We compared the structure of the NBD in complex with the AtBAG1 UBD with that of the ADP-bound NBD (PDB entry 1hjo; Osipiuk *et al.*, 1999; Supplementary Fig. S3*a*). The ADP-bound NBD adopts a closed state in which subdomains IB and IIB approach each other. In contrast, binding of the AtBAG1 UBD to the NBD resulted in a rotation of subdomain IIB by approximately 15° relative to subdomain IB, which leads to an opening of the nucleotide-binding cleft. We also compared the AtBAG1 UBD-bound NBD structure with previously reported structures of the NBD in complex with mammalian BDs. The conformation of the NBD complexed with the AtBAG1 UBD is very similar to that of the NBD in complex with the mammalian BAG1 BD (PDB entry 1hx1; Supplementary Fig. S3*b*; Sondermann *et al.*, 2001) and the open form of the NBD bound to BAG5 BD5 (PDB entry 3a8y; Arakawa *et al.*, 2010), with r.m.s.d.s of 0.72 and 0.95 Å, respectively. In the case of BAG2, BAG2 BNB binding also leads to an open NBD state with the displacement of domain II from domain I as a single unit without altering the relative orientation of subdomains IIB and IB. Comparison of the BNB-bound and AtBAG1 UBD-bound structures of the Hsc70 NBD indicates that the AtBAG-bound Hsc70 NBD structure is distinct from the BAG2-bound structure (Supplementary Fig. S3*c*).

The interaction between the AtBAG proteins and Hsc70 was confirmed by *in vitro* pull-down assays. AtBAG1–4 BDs tagged with haemagglutinin (HA) were assayed for the ability to bind GST-fused AtHsc70 NBD produced in *E. coli*. The results revealed that the AtBAG1–4 BDs all interact with GST-fused AtHsc70 NBD but not with GST (Supplementary Fig. S6). Together with the structural homology data, this result indicates that the Hsc70-binding modes of AtBAG1–4 are conserved.

3.3. AtBAG proteins function as Hsc70 nucleotide-exchange factors

We assessed the effect of the AtBAG BD on the affinity of the NBD for ADP using isothermal titration calorimetry (ITC) assays. The NBD fragment solution (20 μM) was first titrated with the ADP solution (400 μM). The curve of the heat changes was fitted using a single-site binding model and demonstrated an affinity of 57.1 nM (Fig. 3*a*). Next, we titrated AtBAG1 BD–NBD solution (20 μM) with the ADP solution (400 μM). The significantly decreased equilibrium dissociation constants (K_d = 2.5 μM) indicated that binding of the AtBAG1 BD reduced the affinity of the NBD for ADP (Fig. 3*b*). The NBD complexed with the AtBAG2–4 BDs had a similarly reduced affinity for ADP, with K_d values of 1.8, 2.4 and 4.5 μM, respectively (Figs. 3*c*, 3*d* and 3*e*). Excess ATP is present in the cytosol. Hsp70 and Hsc70 fulfil their chaperone activity by cycling between ATP-bound and ADP-bound states (Bukau & Horwich, 1998). Hsp70 and Hsc70 release ADP at quite a low rate (Jiang *et al.*, 2005). These data suggested that the AtBAG1–4 BDs might facilitate the release of ADP from the NBD and accelerate the ATP cycle through direct interaction with the NBD, indicating that the AtBAG proteins function as nucleotide-exchange factors in plants.

3.4. The ubiquitin-like domain in AtBAG proteins

Despite the low sequence identity (14.3%) between the AtBAG1 ubiquitin-like domain (ULD) and human ubiquitin

(referred to as hsUB; Fig. 4*a*), the AtBAG ULD adopts a characteristic ubiquitin fold that contains three α-helices and a mixed β-sheet containing four strands (Fig. 4*b*). The hsUB structure (PDB entry 1ubq; Vijay-Kumar *et al.*, 1987) superimposed very well onto the AtBAG1 ULD structure, with an r.m.s.d. value of 0.99 Å. Lys48 of hsUB, which is critical in the proteolytic function, is conserved in AtBAG1 ULD as Lys113 (Fig. 4*c*).

In the AtBAG1 UBD–NBD complex structure, the ULD is connected to the BD by a loop and lies extended away from the NBD (Fig. 2*a*). However, the ULD is involved in crystal contacts with the BD and the NBD of neighbouring molecules (Supplementary Fig. S4). These contacts might fix the flexible connection between the ULD and the BD and facilitate the crystal packing of the complex, which may explain the failure of the AtBAG1 UBD alone to crystallize. We further examined whether these crystal contacts were functional. The result of the ultracentrifugation experiment indicated the presence of a homogenous monomer of the AtBAG1 UBD–NBD complex in solution (Fig. 4*d*), suggesting that the intermolecular crystal contacts were not likely to change the monomeric state of the complex. ITC assays indicated that the

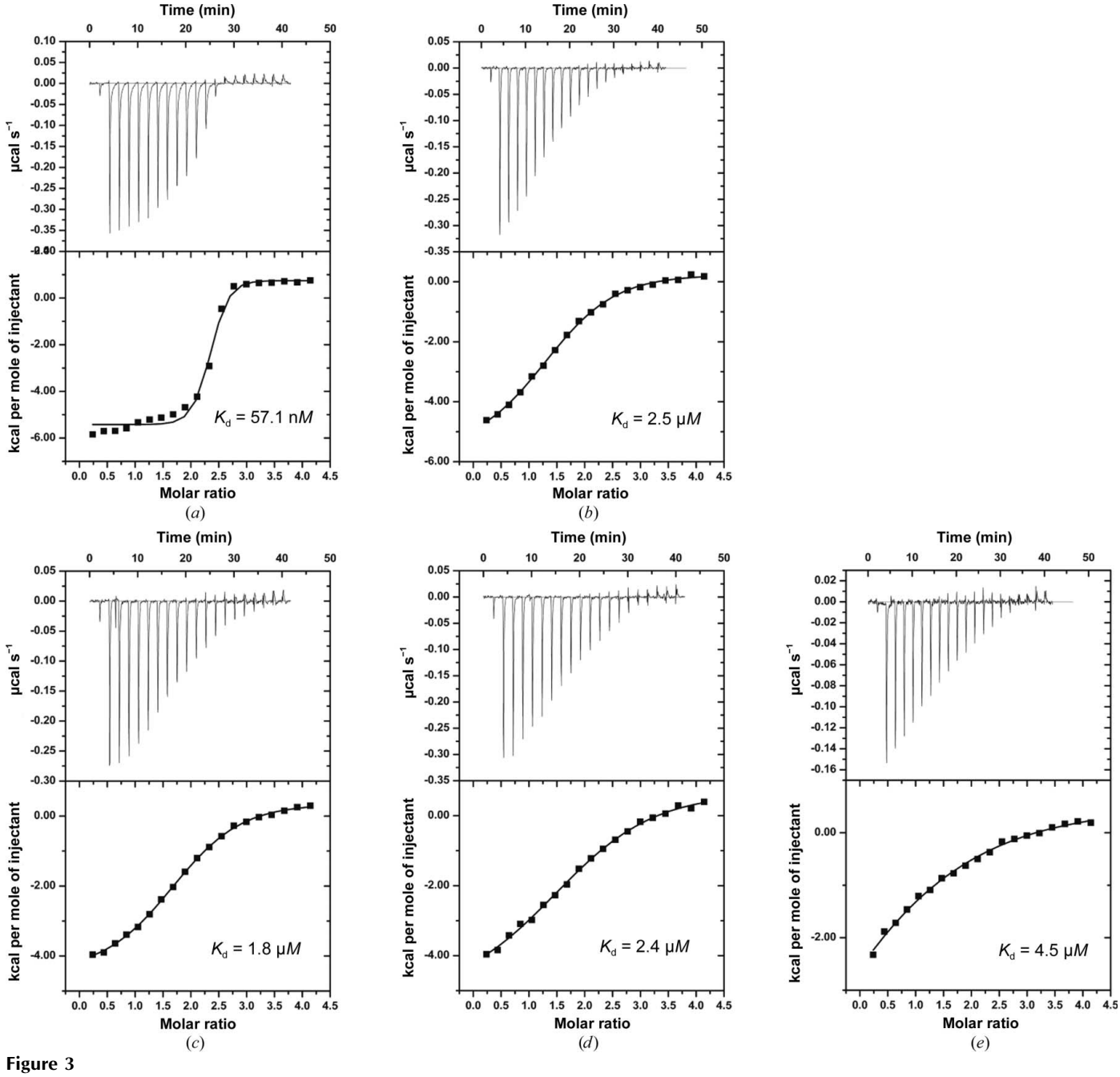

Figure 3
The AtBAG14 BDs reduce the affinity of the NBD for ADP. ITC analysis of the interaction of the NBD alone with ADP (*a*), the NBD with ADP in the presence of the AtBAG1 BD (*b*), the NBD with ADP in the presence of the AtBAG2 BD (*c*), the NBD with ADP in the presence of the AtBAG3 BD (*d*) and the NBD with ADP in the presence of the AtBAG4 BD (*e*).

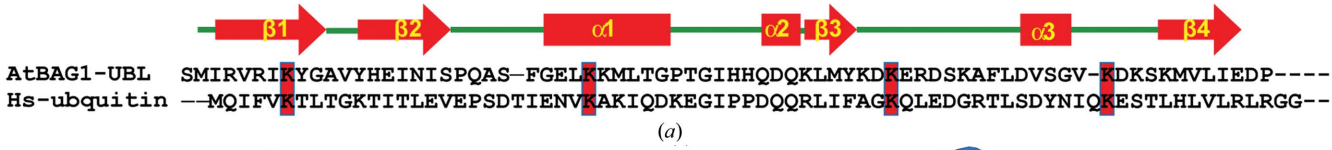

(*a*)

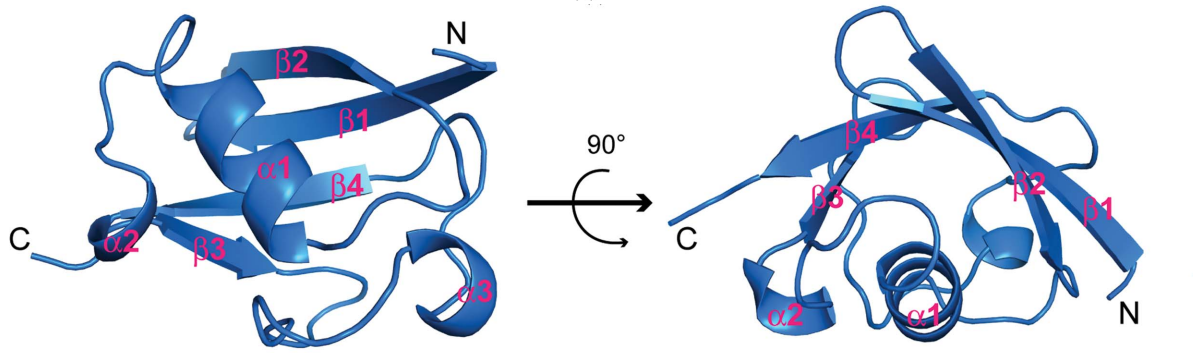

(*b*)

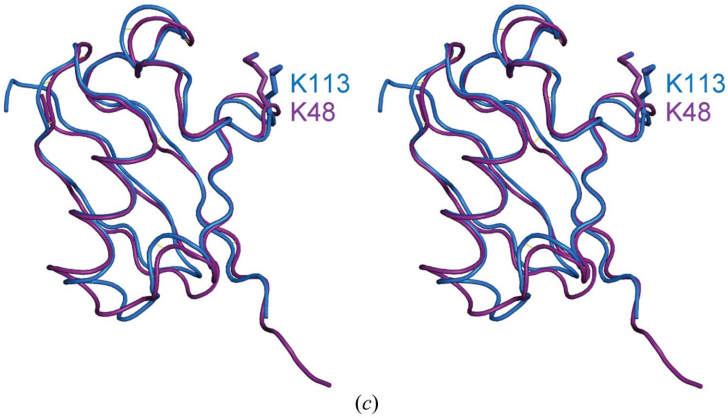

(*c*)

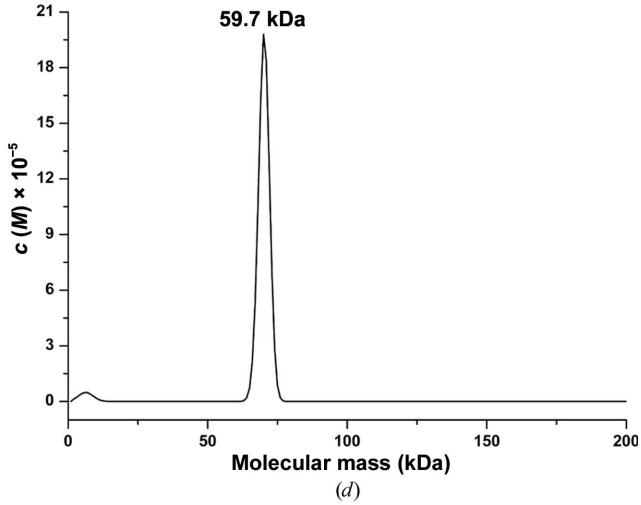

(*d*)

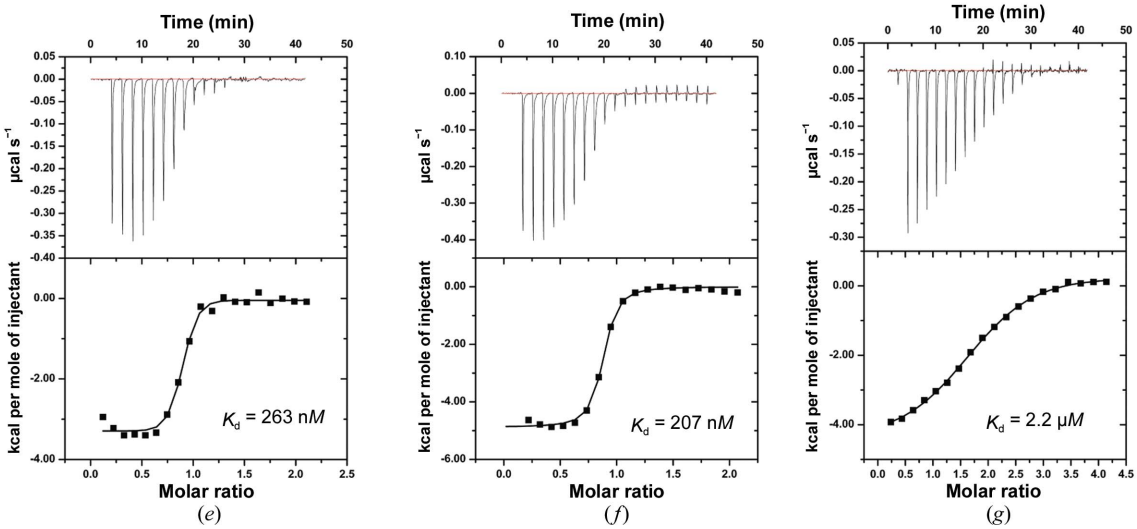

(*e*) (*f*) (*g*)

Figure 4
Structure of the AtBAG1 ULD. (*a*) Structure-based sequence alignment of the AtBAG1 ULD with human ubiquitin. The conserved lysine residues are boxed in red. The locations of the secondary-structural features are shown above the alignment. (*b*) Overall structure of the AtBAG1 ULD. (*c*) Stereoview of the superposition of the AtBAG1 ULD (marine) and human ubiquitin (PDB entry 1ubq; purple). The side chains of Lys113 of AtBAG1 and the corresponding Lys48 of human ubiquitin are shown. (*d*) Sedimentation-velocity analysis of the AtBAG1 UBD–NBD complex at 42 000 rev min^{-1} and 277 K. The mass estimate suggests that the complex is a monomer with a molecular weight of 59.7 kDa. (*e*) ITC analysis of the interaction of the AtBAG1 BD with the NBD. (*f*) ITC analysis of the interaction of the AtBAG1 UBD with the NBD. (*g*) ITC analysis of the interaction of the NBD with ADP in the presence of the AtBAG1 UBD.

AtBAG1 UBD and the AtBAG1 BD bind to the NBD with similar affinities (263 and 207 n*M*, respectively; Fig. 4*e*) and that the affinity of the AtBAG1 UBD-bound NBD for ADP was reduced to 2.1 µ*M* (Fig. 4*f*), suggesting that the AtBAG1 UBD has an effect similar to that of the AtBAG1 BD in accelerating the nucleotide exchange of Hsc70. Furthermore, the gradient GST pull-down assay indicated the same level of binding of AtHsc70 to the AtBAG1 BD and the AtBAG1 UBD (Supplementary Fig. S6). Taken together, these results indicate that it is possible that the ULD has little effect on the cochaperone function of the AtBAG proteins.

3.5. Characterization of an AtBAG2 T-DNA insertion mutant

To elucidate the biological role of AtBAGs *in vivo*, T-DNA insertion lines of AtBAG2, AtBAG2 and AtBAG4 were obtained from ABRC. Only the AtBAG2 insertion line SALK_030295 was confirmed by PCR as having the T-DNA insertion and was named *bag2-1*. The T-DNA insertion in *bag2-1* is located in AtBAG2 exon 4 (Fig. 5*a*). RT-PCR with gene-specific primers showed that the AtBAG2 transcription level was reduced in the *bag2-1* mutant (Fig. 5*b*). We did not note any morphological defects in the *bag2-1* mutant, and the *bag2-1* mutant plant seemed larger than the wild-type plants (Figs. 5*c*, 5*d* and 5*g*). We performed quantification on five-day-old seedlings and four-to-five-week-old plants. The root lengths and hypocotyl lengths of 18 five-day-old seedlings were measured. The average root length of wild-type seedlings was 7.8 mm, whereas the average root length of *bag2-1* mutant seedlings was 8.6 mm; they differed significantly according to the t-test (P = 0.08; Fig. 5*e*). The average hypocotyl length of wild-type and *bag2-1* mutant seedlings were not significantly different according to the t-test (wild type = 1.245 mm; *bag2-1* = 1.271 mm; P = 0.3; Fig. 5*f*). The rosette sizes of 20 four-to-five-week-old plants were quantified; the results showed that both rosettes of four-to-five-week-old *bag2-1* mutants plants were significantly larger than those of the wild type according to the t-test (wild type = 7.4 and 9.2 cm;

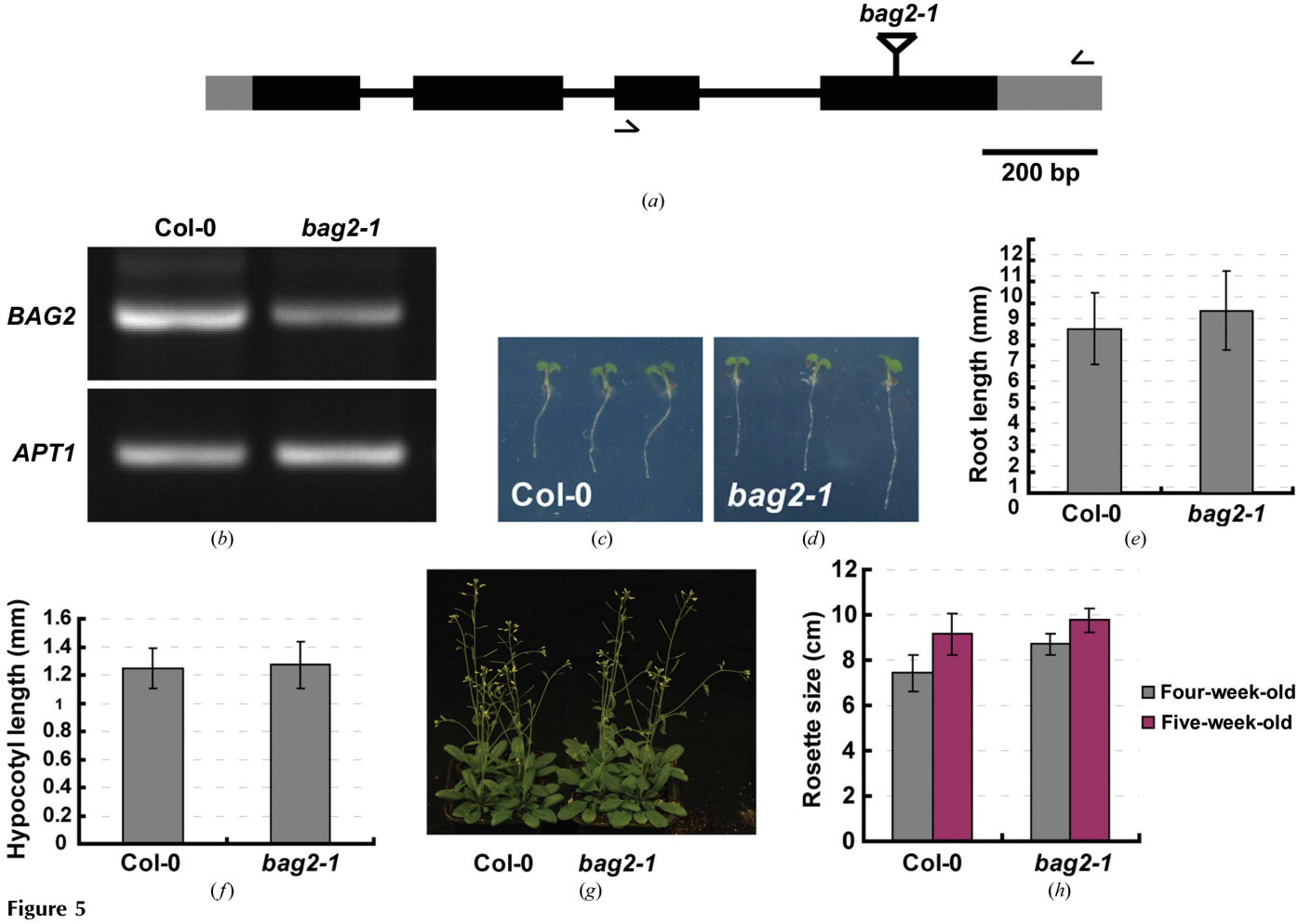

Figure 5
Isolation and characterization of the *bag2-1* mutant. (*a*) Schematic representation of the T-DNA insertion into the fourth exon of the AtBAG2 locus (At5g62100; triangle). Black boxes represent exons, grey boxes represent UTRs, black lines represent introns and arrows represent RT-PCR primers; the scale bar corresponds to 200 bp. (*b*) Semi-quantitative RT-PCR analysis of wild-type (wt) Col-0 and the *bag2-1* mutant; the *APT1* gene was used as a reference control. (*c*, *d*) Comparison of five-day-old wt and *bag2-1* mutant seedlings. (*e*, *f*) Quantitative analyses of the root length and hypocotyl length of five-day-old wt and *bag2-1* mutant seedlings, average ± SD, n = 18. (*g*) Comparison of five-week-old wt and *bag2-1* mutant plants. (*h*) Quantification of the rosette sizes of four- and five-week-old plants, average ±SD, n = 20.

bag2-1 = 8.7 and 9.8 cm; $P = 1.4 \times 10^{-7}$ and 0.007; Fig. 5*h*). Our data suggest that the BAG proteins influence plant growth and development.

4. Discussion

We have determined that the BD in the AtBAG1–4 proteins adopts the antiparallel three-helix bundle, which is similar to the short BAG structure of mammalian BAG3, BAG4 and BAG5. We also provided direct evidence that the Hsc70-binding mode of the AtBAG1–4 proteins is similar to that of mammalian BAG1 and BAG5 BD5. The similar opening of the nucleotide-binding cleft induced by the binding of the AtBAG proteins suggests a conserved cochaperone activity of the AtBAG proteins (Supplementary Fig. S5). In plants, increased Hsp70/Hsc70 expression is associated with decreased plant PCD caused by abiotic stresses, including heat/cold stress, salt stress and heavy-metal stress (Wang *et al.*, 2004). The increased level of Hsp70/Hsc70 correlates with the PCD-based HR response, which is deeply involved in defence against pathogen attack (Snyman & Cronjé, 2008; Duan *et al.*, 2011). Hsp70/Hsc70 also play essential roles in plant development, including root growth, seed maturation and germination, and leaf growth (Su & Li, 2008). Our structural and biochemical data demonstrate that the AtBAG proteins function as nucleotide-exchange factors for Hsp70/Hsc70 in plants and provide a possible explanation for the multiple functions of AtBAG4 in plant growth, development and stress responses.

A feature of AtBAG1–4 is the presence of the N-terminal ULD, which is also found in mammalian BAG1 (Takayama *et al.*, 1999). Mammalian ubiquitin has multiple functions, including membrane trafficking, protein kinase activation, DNA repair and targeting protein destruction by the 26S proteasome (Pickart, 2004; Chen & Sun, 2009). Previous studies of mammalian BAG1 found that the ULD serves as an integral sorting signal to stimulate interaction of BAG1 with the proteasome (Lüders, Demand & Höhfeld, 2000; Lüders, Demand, Papp *et al.*, 2000; Alberti *et al.*, 2002). Increasing the cellular levels of BAG1 stimulates association of Hsc70 with the proteasome (Luders *et al.*, 2000). Moreover, BAG1 and CHIP can simultaneously associate with Hsc70. The ternary BAG1–Hsc70–CHIP complex facilitates the attachment of a polyubiquitin chain to BAG-1 and thereby promotes the association of the chaperone complex with the proteasome (Alberti *et al.*, 2002). Our structural data indicate that the AtBAG ULD adopts a characteristic ubiquitin structure that embraces a precisely conserved lysine corresponding to Lys48 of ubiquitin, which is critical in the proteolytic function of ubiquitin (Petroski & Deshaies, 2005). Orthologues of CHIP and ubiquitin ligase complexes have been identified in *A. thaliana* (Yan *et al.*, 2003; Figueroa *et al.*, 2005). It is tempting to speculate that the AtBAG proteins may fulfill a mammalian BAG1-like function in certain degradation pathways.

Owing to their immobile nature, plants have evolved a large genetic redundancy, which allows them to quickly adapt to the changing environment (Briggs *et al.*, 2006). The AtBAG1–4 proteins are all predicted to localize in the cytoplasm (Doukhanina *et al.*, 2006). Given the high homology of the AtBAG1–4 BD structures and their similar biochemical characteristics with regard to Hsc70 nucleotide exchange, it is likely that the AtBAG1–4 proteins are functionally redundant. Additionally, the proteins may function under different conditions and in different tissues. Our present study suggested that the AtBAG proteins function as nucleotide-exchange factors for Hsp70/Hsc70 in plants. Moreover, our *in vivo* studies showed that *bag2-1* mutant plants are larger than wild-type plants when growing under normal conditions, indicating that AtBAG1–4 might regulate plant PCD and confer tolerance to stresses in plants, as stress tolerances are energy-consuming processes. Further studies of the specific expression patterns and functional roles of each of the AtBAG family members would facilitate an understanding of the mechanism by which the AtBAG family confers stress tolerance in plants. AtBAG5–7 have different domain organizations and divergent locations in plant cells. Further study of the structural and functional determination of the other AtBAG proteins would facilitate a better understanding of the mechanism underlying plant PCD regulation.

We are grateful to Ms Jing Chen and Ms Hui Wei for help in protein purification and crystallization, to Mr Zheng Wang for help with the analytical ultracentrifugation experiment and to the staff of beamline BL-17U1 at the Shanghai Synchrotron Radiation Facility and to the staff of beamline 3W1A at the Beijing Synchrotron Radiation Facility for excellent technical assistance during data collection. This work was funded by the 973 Program (grants 2012CB917200 and 2013CB910400) and the NSFC (grants 31170684 and 91017009).

References

Adams, P. D. *et al.* (2010). *Acta Cryst.* D**66**, 213–221.
Alberti, S., Demand, J., Esser, C., Emmerich, N., Schild, H. & Hohfeld, J. (2002). *J. Biol. Chem.* **277**, 45920–45927.
Arakawa, A., Handa, N., Ohsawa, N., Shida, M., Kigawa, T., Hayashi, F., Shirouzu, M. & Yokoyama, S. (2010). *Structure*, **18**, 309–319.
Arnold, K., Bordoli, L., Kopp, J. & Schwede, T. (2006). *Bioinformatics*, **22**, 195–201.
Baker, N. A., Sept, D., Joseph, S., Holst, M. J. & McCammon, J. A. (2001). *Proc. Natl Acad. Sci. USA*, **98**, 10037–10041.
Briggs, G. C., Osmont, K. S., Shindo, C., Sibout, R. & Hardtke, C. S. (2006). *Trends Plant Sci.* **11**, 492–498.
Bukau, B. & Horwich, A. L. (1998). *Cell*, **92**, 351–366.
Chen, Z. J. & Sun, L. J. (2009). *Mol. Cell*, **33**, 275–286.
Doukhanina, E. V., Chen, S., van der Zalm, E., Godzik, A., Reed, J. & Dickman, M. B. (2006). *J. Biol. Chem.* **281**, 18793–18801.
Duan, Y.-H., Guo, J., Ding, K., Wang, S.-J., Zhang, H., Dai, X.-W., Chen, Y.-Y., Govers, F., Huang, L.-L. & Kang, Z.-S. (2011). *Mol. Biol. Rep.* **38**, 301–307.
Emsley, P. & Cowtan, K. (2004). *Acta Cryst.* D**60**, 2126–2132.
Figueroa, P., Gusmaroli, G., Serino, G., Habashi, J., Ma, L., Shen, Y., Feng, S., Bostick, M., Callis, J., Hellmann, H. & Deng, X. W. (2005). *Plant Cell*, **17**, 1180–1195.
Jiang, J., Prasad, K., Lafer, E. M. & Sousa, R. (2005). *Mol. Cell*, **20**, 513–524.
Kang, C. H. *et al.* (2006). *Cell Death Differ.* **13**, 84–95.
Kiefer, F., Arnold, K., Künzli, M., Bordoli, L. & Schwede, T. (2009). *Nucleic Acids Res.* **37**, D387–D392.

Kuriyama, H. & Fukuda, H. (2002). *Curr. Opin. Plant Biol.* **5**, 568–573.
Lüders, J., Demand, J. & Höhfeld, J. (2000). *J. Biol. Chem.* **275**, 4613–4617.
Lüders, J., Demand, J., Papp, O. & Höhfeld, J. (2000). *J. Biol. Chem.* **275**, 14817–14823.
Mayer, M. P. & Bukau, B. (2005). *Cell. Mol. Life Sci.* **62**, 670–684.
McCoy, A. J., Grosse-Kunstleve, R. W., Adams, P. D., Winn, M. D., Storoni, L. C. & Read, R. J. (2007). *J. Appl. Cryst.* **40**, 658–674.
Osipiuk, J., Walsh, M. A., Freeman, B. C., Morimoto, R. I. & Joachimiak, A. (1999). *Acta Cryst.* D**55**, 1105–1107.
Otwinowski, Z. & Minor, W. (1997). *Methods Enzymol.* **276**, 307–326.
Panter, S. & Dickman, M. (2005). *Cell Engineering*, Vol. 4, edited by M. Al-Rubeai & M. Fussenegger, pp. 107–152. Dordrecht: Kluwer Academic Publishers.
Pape, T. & Schneider, T. R. (2004). *J. Appl. Cryst.* **37**, 843–844.
Pennell, R. I. & Lamb, C. (1997). *Plant Cell*, **9**, 1157–1168.
Petroski, M. D. & Deshaies, R. J. (2005). *Cell*, **123**, 1107–1120.
Pickart, C. M. (2004). *Cell*, **116**, 181–190.
Rayment, I. (1997). *Methods Enzymol.* **276**, 171–179.
Schuck, P. (2000). *Biophys. J.* **78**, 1606–1619.
Snyman, M. & Cronjé, M. J. (2008). *J. Exp. Bot.* **59**, 2125–2132.
Sondermann, H., Scheufler, C., Schneider, C., Hohfeld, J., Hartl, F. U. & Moarefi, I. (2001). *Science*, **291**, 1553–1557.
Su, P.-H. & Li, H. (2008). *Plant Physiol.* **146**, 1231–1241.
Takayama, S., Sato, T., Krajewski, S., Kochel, K., Irie, S., Millan, J. A. & Reed, J. C. (1995). *Cell*, **80**, 279–284.
Takayama, S., Xie, Z. & Reed, J. C. (1999). *J. Biol. Chem.* **274**, 781–786.
Vijay-Kumar, S., Bugg, C. E. & Cook, W. J. (1987). *J. Mol. Biol.* **194**, 531–544.
Walter, T. S., Meier, C., Assenberg, R., Au, K. F., Ren, J., Verma, A., Nettleship, J. E., Owens, R. J., Stuart, D. I. & Grimes, J. M. (2006). *Structure*, **14**, 1617–1622.
Wang, W., Vinocur, B., Shoseyov, O. & Altman, A. (2004). *Trends Plant Sci.* **9**, 244–252.
Williams, B., Kabbage, M., Britt, R. & Dickman, M. B. (2010). *Proc. Natl Acad. Sci. USA*, **107**, 6088–6093.
Wiseman, T., Williston, S., Brandts, J. F. & Lin, L.-N. (1989). *Anal. Biochem.* **179**, 131–137.
Xu, Z., Page, R. C., Gomes, M. M., Kohli, E., Nix, J. C., Herr, A. B., Patterson, C. & Misra, S. (2008). *Nature Struct. Mol. Biol.* **15**, 1309–1317.
Yan, J., Wang, J., Li, Q., Hwang, J. R., Patterson, C. & Zhang, H. (2003). *Plant Physiol.* **132**, 861–869.